Using an Inertial Navigation System (INS) and a Laser Range Finder (LRF) to create a novel Electronic Navigational Aid (ENA) for the blind

Isabelle Chong

Abstract

The current navigation aid of choice for the blind is the white cane, which, although lightweight and easy to acquire, has a limited range and requires extensive training to use. While Electronic Navigational Aids (ENAs) have been developed to improve upon the white cane, the need for certain environmental conditions and preconfigured infrastructure in some approaches (e.g., radio frequency identification and structured light) remains an issue. My objectives were to (1) design the conceptual and mathematical methodology of an ENA for device location and obstacle detection without the use of preconfigured infrastructure, (2) build an ENA by combining a Laser Range Finder (LRF) and an Inertial Navigation System (INS), (3) code a real-time algorithm for obstacle detection and Kalman filtering in C++, and (4) test my ENA's functionality from both an engineering and human subjects standpoint to obtain quantitative and qualitative feedback. The completed ENA can detect obstacles within a six meter range without preconfigured infrastructure, raising an alarm to the user through sound and haptic feedback if an obstacle has been detected. This device has the potential to provide a robust alternative method of blind navigation in the future.

1 Introduction

285 million people are estimated to be visually impaired worldwide, of which 39 million are estimated to be completely blind. This number continues to grow due to the rising age index and the increasingly common occurrence of chronic eye diseases, meaning that more and more people are having to learn how to navigate the world without sight (World Health Organization, 2014). The most common method of blind navigation is the white cane. Although lightweight, easy to acquire, and effective, the white cane has a limited range

Figure 1. My hand-held navigational aid for the blind. The test obstacle is a soft toy for safety reasons. (Graphic by Author)

(approximately 1.0-1.5 m (UltraCane, 2011)) and can be difficult to learn, providing limited information to the user and requiring extensive practice and training to handle correctly (Soong, Lovie-Kitchin, & Brown, 2001). In this study, I have designed and prototyped a hand-held Electronic Navigational Aid (ENA) that detects obstacles in front of a user at a range of up to six meters without the use of preconfigured infrastructure (Figure 1).

1.1 Existing Electronic Navigational Aids

Vision is a difficult sense to replace due to its high bandwidth. Therefore, a successful blind navigation approach aims to increase "bandwidth" for the user. Some approaches to blind navigation use computer vision, a high data processing bandwidth technology (Praveen & Paily, 2013). Simultaneous Location and Mapping (SLAM) approaches compare the movements of recognizable features within a series of images in order to calculate the movement of a user within an environment (Durrant-Whyte & Bailey, 2006). However, such approaches are computationally expensive, and require the use of powerful (laptop sized) computers, making SLAM devices too bulky for regular consumer use (Praveen & Paily, 2013; Tamjidi, Ye, & Hong, 2013). ENAs using structured light sensors have lower computational demands but can only be used indoors because sunlight interferes with their function (Filipe et al., 2012).

Ultrasound approaches are also common in blind navigation, but suffer from a lack of precision because of wide sensor beam width (Borenstein & Ulrich, 1997; *UltraCane*, 2016). Effective approaches to robotic two-dimensional navigation fuse data from an Inertial Navigation System (INS) with data from a Laser Range Finder (LRF) through a Kalman filter algorithm (Travis, Simmons, & Bevly, 2005), suggesting an approach to blind navigation that combines an INS and LRF or other laser-based system in a smaller, hand-held, three-dimensional capable system (Dang, Chee, Pham, & Suh, 2016).

My ENA functions on two unique concepts: floor detection and relative height finding. Rather than identifying many different types of obstacles, which is impractical and computationally expensive (Chen, Pau, & Wang, 1993), the ENA detects obstacles using height profiles. A deviation from the expected height profile causes the device to sound an alarm. The device does not concern itself with where exactly the user is; instead, it finds whether or not an obstacle is in the user's path. This is an important improvement over existing ENAs because the simplified algorithms are less computationally demanding and therefore allow the use of smaller, lighter components at a lower price point.

2   Objectives

Table 1 lists the objectives for creating a hand-held ENA that allows the blind to safely avoid obstacles without the use of preconfigured infrastructure.

Table 1
Objectives for building and testing an ENA.

	Objective	Description
1	Conceptual	Develop and design algorithms to calculate the location of a user in 3D space, detect obstacles within an environment, and filter noise from measurements
2	Hardware	Design and prototype an ENA that combines an INS with a LRF to detect obstacles in 3D space
3	Software	Program a real-time Kalman Filter noise reduction algorithm using C++ and cross compile onto a BeagleBone Black microprocessor. Use an algorithm to integrate INS and LRF sensor data and determine the presence of obstacles
4	Engineering Testing	Check (i) sampling speed, (ii) range and (iii) operational performance using real-time telemetry
5	Field Trials	Obtain quantitative and qualitative feedback from human subjects regarding the functioning of the ENA

3 Methods

3.1 Overview

I designed and built the prototype ENA in my basement laboratory (Figure 11.a), incorporating a custom designed surface-mount PCB, and wrote the C++ program that controls the ENA. My mentor assisted me with the device's mathematical algorithm, and my parents were supervisory adults who ensured my safety and helped me learn to use power tools.

Figure 2 shows an overview of the ENA's obstacle detection process. There are four parts to the ENA's detection algorithm: (1) reading and processing sensor parameters, (2) calculating the attitude and height of the ENA[1] in 3D space using a Kalman filter, (3) determining the height of the laser spot shining on a floor/obstacle, and (4) sounding an alarm based on that laser spot's height profile.

Figure 2. Block diagram of ENA, including electronic devices used and the associated concepts (Graphic by Author).

3.2 Sensor parameter calculations

The ENA uses a Bosch BNO055 Micro Electrical Mechanical Sensor (MEMS) INS. INS units are typically used to track locations in 3D-space (Draper, 1981; Wrigley, 1977). The BNO055 has nine degrees of freedom from (1) Gyroscopes, (2) Accelerometers and (3) Magnetometers. The choice of MEMS INS used in the ENA is primarily dictated by cost, requiring the ENA's algorithm to accommodate more noise because cheaper INS sensors are more noisy (Titterton & Weston, 2004).

The ENA's position in 3D space is tracked over time using accelerometer readings from the BNO055 INS and integrating them twice. Because acceleration measurements from the INS

---

[1]The ENA's position reference point for calculation purposes is defined as the BNO055 INS integrated circuit chip mounted on the green printed circuit board (Figure 4.b)
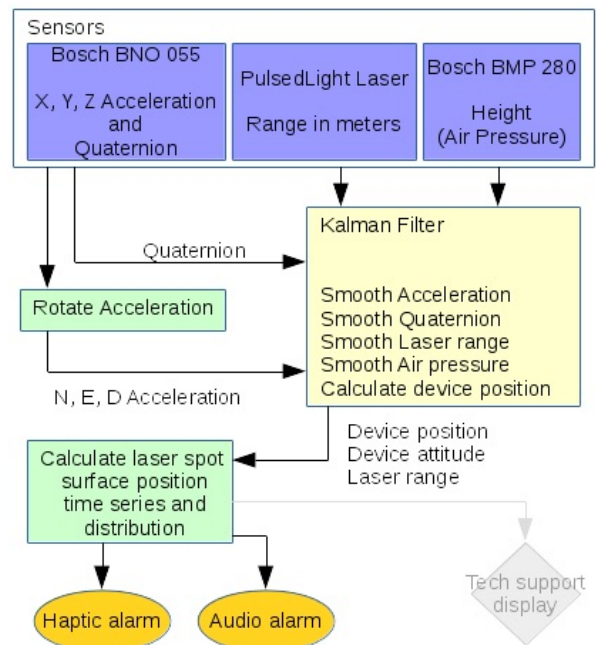
are with respect to the ENA's axis, the Body Frame, they must first be rotated into the North East Down (NED) Frame before being entered into the Kalman filter equation (Noureldin, Karamat, & Georgy, 2013). This is done using quaternion measurements from the BNO055 and applying a Hamiltonian product to the body frame acceleration vectors (Hamilton, 1844; Diebel, 2006). Quaternions are used as opposed to Euler Angles because quaternions are immune to gimbal lock (*Understanding Quaternions*, 2016).

Additional information regarding the height of the ENA in 3D space is given by the BMP280 pressure sensor that measures air pressure ψ in Pascals, which is then converted to relative height $p_{d,m}$ (Table 3) in meters[2] by Equation 3. Equation 1 assumes that $h = 0$ m (at sea level), a_0 = sea level atmospheric pressure (101325 Pa), T_0 = sea level standard temperature (288.15 K), g = Earth-surface gravitational acceleration (9.80665 m/s^2), M = molar mass of dry air (0.0289644 kg/mol), and R = universal gas constant (8.31447 $J/(mol \cdot K)$) and relates air pressure to altitude (Wikipedia B, 2016):

$$a = a_0 \left(1 - \frac{Lh}{T_0} \right)^{\frac{gM}{RL}} \quad (1) \qquad \left. \frac{\partial a}{\partial h} \right|_{h=0} = -\frac{a_0 LgM}{T_0 RL} = -12.0130 \quad (2)$$

By taking the partial derivative of Equation 1 with respect to altitude and substituting in the known values, the change in atmospheric pres-

$$p_{d,m} = (\psi - \psi_r) \times 0.0832 \quad (3)$$

sure with respect to the change in height is calculated (Equation 2). The engineering approximation calculated from this partial derivative, 0.0832 in Equation 3[3], is then multiplied by the difference between ψ, the BMP280 air pressure reading in Pascals, and ψ_r, the air pressure reference reading recorded during the startup sequence of the ENA, to calculate relative height, $p_{d,m}$ (Equation 3).

However, noise must be first be removed from the sensor measurements before further calculations for obstacle location can be performed.

---

[2]Note the convention is $p_{d,m}$ position *down* increases in value the lower the position is.
[3]$1/12.0130 \approx 0.0832$ m/Pa

3.3 Kalman filter noise reduction, ENA attitude and height calculations

For any MEMS INS device utilizing sensors, there is a degree of noise within measurements. This noise is assumed to be Gaussian and proportional to the square root of the sampling rate (Looney, 1995-2016). It was found that sampling at 100Hz, the default BNO055 sampling rate, was a good compromise between noise and data rate. Small MEMS devices may also exhibit issues regarding accelerometer drift. Such issues must be accounted for as well, especially when integrating measurements, as the act of integrating causes the amount of drift to grow.

3.3.1 Drift. The BNO055 has a gravity correction vector that ensures that the acceleration due to gravity is subtracted from the Down accelerometer reading. The gravity vector's position is often skewed because of gyroscope error (Woodman, 2007), leading to a bias, which can be considered a low-frequency noise. Surprisingly, a bias of just two degrees sustained over 10 seconds causes a horizontal North / East position drift error of 17.1 meters; however, the down drift error is significantly smaller at just 30 centimeters. Assuming acceleration due to gravity $g = 9.81 \, m/s^2$:

$$a_n = g * sin(\theta) \qquad (4) \qquad\qquad a_d = g * (1 - cos(\theta)) \qquad (6)$$

$$\left. \frac{da_n}{d\theta} \right|_{\theta=0} = 9.81 \, m/s^2 \qquad (5) \qquad\qquad \left. \frac{da_d}{d\theta} \right|_{\theta=0} = 0 \, m/s^2 \qquad (7)$$

The difference in sensitivity is explained by Equations 4 to 7, the sensitivity of horizontal acceleration (North) a_n being greater than that of acceleration down a_d for an error in θ, when $\theta \approx 0$. In order to correct for this drift, a high-pass filter was implemented (Equation 8) (Smith, 2008)

$$y_t = \alpha y_{t-1} + (x_t - x_{t-1}) \qquad (8) \qquad\qquad f_c = \frac{1 - \alpha}{2\pi\alpha\Delta t} \qquad (9)$$

where y_t is the output at time t, x_t is the input at time t, and $t-1$ indicates the previous time sample. α must be between 0 and 1 and was determined empirically in this case to be 0.999 (Section 4.1.3). The formula for f_c (Equation 9) determines the cut-off frequency of the filter and was calculated to be 0.0159 Hz (Table 9).

A BMP280 pressure sensor was also used to provide an absolute reading for elevation that was converted into a height reading (Equation 3, and variable $p_{d,m}$ in Table 3). This height

Table 2
Kalman filter state variables

Index	Variable	Description
0	p_n	Position in the Navigation Frame, North, meters
1	v_n	Velocity in the Navigation Frame, North, meters per second
2	a_n	Acceleration in the Navigation Frame, North, meters per second squared
3	p_e	Position in the Navigation Frame, East, meters
4	v_e	Velocity in the Navigation Frame, East, meters per second
5	a_e	Acceleration in the Navigation Frame, East, meters per second squared
6	p_d	Position in the Navigation Frame, Down, meters
7	v_d	Velocity in the Navigation Frame, Down, meters per second
8	a_d	Acceleration in the Navigation Frame, Down, meters per second squared
9	q_0	Quaternion real component
10	q_1	Quaternion imaginary i component
11	q_2	Quaternion imaginary j component
12	q_3	Quaternion imaginary k component
13	D	Laser distance in meters

reading is less susceptible to drift than that calculated from the INSs acceleration readings. Thus, drift in height can be reduced (Tanigawa, Luinge, Schipper, & Slycke, 2008).

3.3.2   Kalman Filter.   The Kalman filter algorithm, in addition to removing noise, executes the double integral to calculate position. Equations 10 through 22 describe the mathematical process for the Kalman filter. It is assumed that all measurements taken are uncorrelated[4], leading to a diagonal covariance matrix **R** of measurement noise (Equation 22). Therefore, a Sequential Kalman Filter can be used to reduce noise and calculate the position of the ENA with increased numerical stability (Simon, 2006; Kalman, 1960)[5] [6]:

$$\mathbf{x}_{k|k-1} = \mathbf{F}\mathbf{x}_{k-1|k-1} + \mathbf{B}\mathbf{u}_k \qquad (10) \qquad\qquad \mathbf{P}_{k|k-1} = \mathbf{F}\mathbf{P}_{k-1}\mathbf{F}^T + \mathbf{Q}_{k-1} \qquad (11)$$

In which $\mathbf{x}_{k|k-1}$ is a fourteen element vector whose elements are described in Table 2, and $\mathbf{P}_{k|k-1}$ is the fourteen by fourteen element state covariance matrix. k indicates the current time sample. $\mathbf{x}_{k-1|k-1}$ indicates the state at time $k-1$, and $\mathbf{x}_{k|k-1}$ indicates the halfway state of the Kalman filter after the predict equations. Given the measurement vector at time k, indicated by $\mathbf{z}_k$ (values listed in Table 3), we iterate by r steps to obtain the next state vector $\mathbf{x}_{k|k}$ and covariance matrix $\mathbf{P}_{k|k}$.

---

[4]The quaternion measurements are not technically independent because each element is normalized. However, because the ENA samples at a rate of 100Hz, the assumption can be made that any quaternion changes are small enough so that each element can still be considered independent.

[5]This paper follows the mathematical notation convention from Wikipedia (Wikipedia A, 2016).

[6]There are no control inputs, **B** and $\mathbf{u}_k$ are set to zero, Equation 10.

Table 3

Kalman filter measurement inputs, $\mathbf{z}$ in Equation 15

Index	Variable	Description
0	$a_{n,m}$	Acceleration in the Navigation Frame, North, meters per second squared
1	$a_{e,m}$	Acceleration in the Navigation Frame, East, meters per second squared
2	$a_{d,m}$	Acceleration in the Navigation Frame, Down, meters per second squared
3	$q_{0,m}$	Quaternion real component
4	$q_{1,m}$	Quaternion imaginary i component
5	$q_{2,m}$	Quaternion imaginary j component
6	$q_{3,m}$	Quaternion imaginary k component
7	D_m	Laser distance measurement in meters
8	$p_{d,m}$	Relative height in meters from BMP 280 pressure sensor

Starting with $i = -1$, set

$$\mathbf{x}_{i,k|k} = \mathbf{x}_{k|k-1} \qquad (12) \qquad\qquad \mathbf{P}_{i,k|k} = \mathbf{P}_{k|k-1} \qquad (13)$$

The algorithm[7] applies each available measurement update shown in Table 3 in turn (Equations 14 through 16), for $i = 0...r$ where $r = 8$. Vector $\mathbf{H}_i$ is the ith row of matrix $\mathbf{H}$ (Equation 21), scalar $\mathbf{R}_i$ is the ith row and ith column element of matrix $\mathbf{R}$ (Equation 22), $\mathbf{K}_{i,k|k}$ is the fourteen element Kalman Gain vector, and scalar $\mathbf{z}_{i,k|k}$ is the ith element of the nine element measurement vector $\mathbf{z}$ (Table 3).

$$\mathbf{K}_{i,k|k} = \frac{\mathbf{P}_{i-1,k|k}\mathbf{H}_i^T}{\mathbf{H}_i\mathbf{P}_{i-1,k|k}\mathbf{H}_i^T + \mathbf{R}_i} \qquad (14)$$

$$\mathbf{x}_{i,k|k} = \mathbf{x}_{i-1,k|k} + \mathbf{K}_{i,k|k}(\mathbf{z}_{i,k|k} - \mathbf{H}_i\mathbf{x}_{i-1,k|k}) \qquad (15)$$

$$\mathbf{P}_{i,k|k} = (\mathbf{I} - \mathbf{K}_{i,k|k}\mathbf{H}_i)\mathbf{P}_{i-1,k|k}(\mathbf{I} - \mathbf{K}_{i,k|k}\mathbf{H}_i)^T + \mathbf{K}_{i,k|k}\mathbf{R}_i\mathbf{K}_{i,k|k}^T \qquad (16)$$

Finally we set the state vector and covariance matrix at time $k|k$:

$$\mathbf{x}_{k|k} = \mathbf{x}_{r,k|k} \qquad (17) \qquad\qquad \mathbf{P}_{k|k} = \mathbf{P}_{r,k|k} \qquad (18)$$

Equation 19 is the Kalman filter state covariance matrix that follows the stochastic integral derivation from (Singhal, Harit, & Vishwakarma, 2012) and (Bar-Shalom, Li, & Kirubarajan, 2004). When these equations are followed, they produce a series of state vectors $\mathbf{x}_{k|k}$ (Equation 17) and covariance matrices $\mathbf{P}_{k|k}$ (Equation 18) over time that will be utilized to detect obstacles.

In these sequential Kalman filter equations, matrix I is a 14 x 14 identity matrix, and matrices $\mathbf{Q}$, $\mathbf{F}$, $\mathbf{H}$, and $\mathbf{R}$ are as follows:

---

[7](Simon, 2006), pages 150 through 155

Table 4

State covariance Q matrix variances

Variable	Description
σ_n^2	Scaling factor variance in state, North
σ_e^2	Scaling factor variance in state, East
σ_d^2	Scaling factor variance in state, Down
$\sigma_{q_0}^2$	First quaternion element variance in state
$\sigma_{q_1}^2$	Second quaternion element variance in state
$\sigma_{q_2}^2$	Third quaternion element variance in state
$\sigma_{q_3}^2$	Fourth quaternion element variance in state
σ_{laser}^2	Laser distance variance in state

$$
\mathbf{Q} = \begin{bmatrix}
\frac{\Delta t^5 \sigma_n^2}{20} & \frac{\Delta t^4 \sigma_n^2}{8} & \frac{\Delta t^3 \sigma_n^2}{6} & 0 & 0 & 0 & 0 & 0 & 0 & 0 & 0 & 0 & 0 & 0 \\
\frac{\Delta t^4 \sigma_n^2}{8} & \frac{\Delta t^3 \sigma_n^2}{6} & \frac{\Delta t^2 \sigma_n^2}{2} & 0 & 0 & 0 & 0 & 0 & 0 & 0 & 0 & 0 & 0 & 0 \\
\frac{\Delta t^3 \sigma_n^2}{6} & \frac{\Delta t^2 \sigma_n^2}{2} & \Delta t \sigma_n^2 & 0 & 0 & 0 & 0 & 0 & 0 & 0 & 0 & 0 & 0 & 0 \\
0 & 0 & 0 & \frac{\Delta t^5 \sigma_e^2}{20} & \frac{\Delta t^4 \sigma_e^2}{8} & \frac{\Delta t^3 \sigma_e^2}{6} & 0 & 0 & 0 & 0 & 0 & 0 & 0 & 0 \\
0 & 0 & 0 & \frac{\Delta t^4 \sigma_e^2}{8} & \frac{\Delta t^3 \sigma_e^2}{6} & \frac{\Delta t^2 \sigma_e^2}{2} & 0 & 0 & 0 & 0 & 0 & 0 & 0 & 0 \\
0 & 0 & 0 & \frac{\Delta t^3 \sigma_e^2}{6} & \frac{\Delta t^2 \sigma_e^2}{2} & \Delta t \sigma_e^2 & 0 & 0 & 0 & 0 & 0 & 0 & 0 & 0 \\
0 & 0 & 0 & 0 & 0 & 0 & \frac{\Delta t^5 \sigma_d^2}{20} & \frac{\Delta t^4 \sigma_d^2}{8} & \frac{\Delta t^3 \sigma_d^2}{6} & 0 & 0 & 0 & 0 & 0 \\
0 & 0 & 0 & 0 & 0 & 0 & \frac{\Delta t^4 \sigma_d^2}{8} & \frac{\Delta t^3 \sigma_d^2}{6} & \frac{\Delta t^2 \sigma_d^2}{2} & 0 & 0 & 0 & 0 & 0 \\
0 & 0 & 0 & 0 & 0 & 0 & \frac{\Delta t^3 \sigma_d^2}{6} & \frac{\Delta t^2 \sigma_d^2}{2} & \Delta t \sigma_d^2 & 0 & 0 & 0 & 0 & 0 \\
0 & 0 & 0 & 0 & 0 & 0 & 0 & 0 & 0 & \sigma_{q_0}^2 & 0 & 0 & 0 & 0 \\
0 & 0 & 0 & 0 & 0 & 0 & 0 & 0 & 0 & 0 & \sigma_{q_1}^2 & 0 & 0 & 0 \\
0 & 0 & 0 & 0 & 0 & 0 & 0 & 0 & 0 & 0 & 0 & \sigma_{q_2}^2 & 0 & 0 \\
0 & 0 & 0 & 0 & 0 & 0 & 0 & 0 & 0 & 0 & 0 & 0 & \sigma_{q_3}^2 & 0 \\
0 & 0 & 0 & 0 & 0 & 0 & 0 & 0 & 0 & 0 & 0 & 0 & 0 & \sigma_{laser}^2
\end{bmatrix}
\tag{19}
$$

$$
\mathbf{F} = \begin{bmatrix}
1 & \Delta t & \frac{\Delta t^2}{2} & 0 & 0 & 0 & 0 & 0 & 0 & 0 & 0 & 0 & 0 & 0 \\
0 & 1 & \Delta t & 0 & 0 & 0 & 0 & 0 & 0 & 0 & 0 & 0 & 0 & 0 \\
0 & 0 & 1 & 0 & 0 & 0 & 0 & 0 & 0 & 0 & 0 & 0 & 0 & 0 \\
0 & 0 & 0 & 1 & \Delta t & \frac{\Delta t^2}{2} & 0 & 0 & 0 & 0 & 0 & 0 & 0 & 0 \\
0 & 0 & 0 & 0 & 1 & \Delta t & 0 & 0 & 0 & 0 & 0 & 0 & 0 & 0 \\
0 & 0 & 0 & 0 & 0 & 1 & 0 & 0 & 0 & 0 & 0 & 0 & 0 & 0 \\
0 & 0 & 0 & 0 & 0 & 0 & 1 & \Delta t & \frac{\Delta t^2}{2} & 0 & 0 & 0 & 0 & 0 \\
0 & 0 & 0 & 0 & 0 & 0 & 0 & 1 & \Delta t & 0 & 0 & 0 & 0 & 0 \\
0 & 0 & 0 & 0 & 0 & 0 & 0 & 0 & 1 & 0 & 0 & 0 & 0 & 0 \\
0 & 0 & 0 & 0 & 0 & 0 & 0 & 0 & 0 & 1 & 0 & 0 & 0 & 0 \\
0 & 0 & 0 & 0 & 0 & 0 & 0 & 0 & 0 & 0 & 1 & 0 & 0 & 0 \\
0 & 0 & 0 & 0 & 0 & 0 & 0 & 0 & 0 & 0 & 0 & 1 & 0 & 0 \\
0 & 0 & 0 & 0 & 0 & 0 & 0 & 0 & 0 & 0 & 0 & 0 & 1 & 0 \\
0 & 0 & 0 & 0 & 0 & 0 & 0 & 0 & 0 & 0 & 0 & 0 & 0 & 1
\end{bmatrix}
\tag{20}
$$

$$\mathbf{H} = \begin{bmatrix} 1 & 0 & 0 & 0 & 0 & 0 & 0 & 0 & 0 & 0 & 0 & 0 & 0 & 0 & 0 \\ 0 & 0 & 0 & 1 & 0 & 0 & 0 & 0 & 0 & 0 & 0 & 0 & 0 & 0 & 0 \\ 0 & 0 & 0 & 0 & 0 & 0 & 1 & 0 & 0 & 0 & 0 & 0 & 0 & 0 & 0 \\ 0 & 0 & 0 & 0 & 0 & 0 & 0 & 0 & 0 & 0 & 1 & 0 & 0 & 0 & 0 \\ 0 & 0 & 0 & 0 & 0 & 0 & 0 & 0 & 0 & 0 & 0 & 1 & 0 & 0 & 0 \\ 0 & 0 & 0 & 0 & 0 & 0 & 0 & 0 & 0 & 0 & 0 & 0 & 1 & 0 & 0 \\ 0 & 0 & 0 & 0 & 0 & 0 & 0 & 0 & 0 & 0 & 0 & 0 & 0 & 1 & 0 \\ 0 & 0 & 0 & 0 & 0 & 0 & 0 & 0 & 0 & 0 & 0 & 0 & 0 & 0 & 1 \\ 0 & 0 & 0 & 0 & 0 & 0 & 1 & 0 & 0 & 0 & 0 & 0 & 0 & 0 & 0 \end{bmatrix} \tag{21}$$

Table 5

Measure covariance R matrix variances

Variable	Description
$\sigma^2_{acc_n,m}$	Variance in acceleration, North
$\sigma^2_{acc_e,m}$	Variance in acceleration, East
$\sigma^2_{acc_d,m}$	Variance in acceleration, Down
$\sigma^2_{q_0,m}$	Variance in first element of quaternion
$\sigma^2_{q_1,m}$	Variance in second element of quaternion
$\sigma^2_{q_2,m}$	Variance in third element of quaternion
$\sigma^2_{q_3,m}$	Variance in fourth element of quaternion
$\sigma^2_{laser,m}$	Variance in laser distance
$\sigma^2_{P_d,m}$	Variance in height calculated by pressure sensor (See equation 3)

$$\mathbf{R} = \begin{bmatrix} \sigma^2_{acc_n,m} & 0 & 0 & 0 & 0 & 0 & 0 & 0 & 0 \\ 0 & \sigma^2_{acc_e,m} & 0 & 0 & 0 & 0 & 0 & 0 & 0 \\ 0 & 0 & \sigma^2_{acc_d,m} & 0 & 0 & 0 & 0 & 0 & 0 \\ 0 & 0 & 0 & \sigma^2_{q_0,m} & 0 & 0 & 0 & 0 & 0 \\ 0 & 0 & 0 & 0 & \sigma^2_{q_1,m} & 0 & 0 & 0 & 0 \\ 0 & 0 & 0 & 0 & 0 & \sigma^2_{q_2,m} & 0 & 0 & 0 \\ 0 & 0 & 0 & 0 & 0 & 0 & \sigma^2_{q_3,m} & 0 & 0 \\ 0 & 0 & 0 & 0 & 0 & 0 & 0 & \sigma^2_{laser,m} & 0 \\ 0 & 0 & 0 & 0 & 0 & 0 & 0 & 0 & \sigma^2_{P_d,m} \end{bmatrix} \tag{22}$$

3.4 Laser spot height and obstacle determination calculations

The LRF's beam shining on a surface in the environment is used to determine the height of floors or obstacles relative to the ENA. The directional cosine matrix ("DCM") represents a 3D rotation and is defined in Equation 23, where the values are obtained from the Kalman filter state

variables (Table 2) (Premerlani & Bizard, 2009).

$$DCM = \begin{bmatrix} q_0^2 + q_1^2 - q_2^2 - q_3^2 & 2q_1q_2 - 2q_0q_3 & 2q_1q_3 + 2q_0q_2 \\ 2q_1q_2 + 2q_0q_3 & q_0^2 - q_1^2 + q_2^2 - q_3^2 & 2q_2q_3 - 2q_0q_1 \\ 2q_1q_3 - 2q_0q_2 & 2q_2q_3 + 2q_0q_1 & q_0^2 - q_1^2 - q_2^2 + q_3^2 \end{bmatrix} \tag{23}$$

$$\begin{bmatrix} s_n \\ s_e \\ s_d \end{bmatrix}_{k|k} = \begin{bmatrix} p_n \\ p_e \\ p_d \end{bmatrix}_{k|k} + D_{k|k} \begin{bmatrix} DCM \end{bmatrix} \begin{bmatrix} l_x \\ l_y \\ l_z \end{bmatrix}_{k|k} \tag{24}$$

The s variables in Equation 24 are the laser spot coordinates. $[l_x, l_y, l_z]^T = [1, 0, 0]^T$ represents the laser vector in the body frame that points straight out of the front of the ENA. The ENA's position variables, p_n, p_e, p_d, and laser distance D are from Table 2. Equation 25 converts Kalman filter noise estimates into surface spot noise estimates.

$$\Omega_k = \mathbf{J}_k \mathbf{P}_k \mathbf{J}_k^T \tag{25}$$

$$\frac{|h_r - s_d|}{\sqrt{\omega_{spot\,down}^2}} > Threshold \tag{26}$$

In which Ω_k (3x3) is the spot covariance matrix at time k, and the Jacobian $\mathbf{J}_k$ is a 3x14 matrix defined in Table 6 and updated at time k. $\mathbf{P}_{k|k}$ is the Kalman state covariance estimate from Equation 18.

A Reference Height h_r is set each time the ENA's trigger is pulled (the "snap time") by setting $h_r = s_{d,snap\,time}$ from Equation 24. This is similar to the Zero Velocity Update method where the Kalman filter is periodically recalibrated with known values (Khairi Abdulrahim & Hill, 2014; Foxlin, 2005). An alarm is then raised if an obstacle has been detected according to Equation 26, where $Threshold$ sensitivity is user set by a dial on the ENA (Figure 6), and noise variable $\omega_{spot\,down}$ is from matrix Ω in Equation 25. False alarms for more distant readings, where the system is less accurate, are suppressed in Equation 26 because $\omega_{spot\,down}$ is larger for those readings.

3.5 Designing and constructing the ENA

Figure 4.a shows an OpenSCAD (Kintel & Clifford Wolf, 2011) rendering of the initial design for the ENA. Figure 3 shows the main components of the ENA, which are integrated via a Printed Circuit Board (PCB). Component names and sources are listed in Table 7. When creating

Table 6

A table of values of the Jacobian matrix $\mathbf{J}_k$ (Equation 25). Matrix values not listed here are zero.

Index	Variable	Matrix element value
0,0	$\frac{\partial s_n}{\partial p_n}$	1
0,1	$\frac{\partial s_n}{\partial v_n}$	Δt
0,2	$\frac{\partial s_n}{\partial a_n}$	$\frac{\Delta t^2}{2}$
0,9	$\frac{\partial s_n}{\partial q_0}$	$2D(l_x q_0 - l_y q_3 + l_z q_2)$
0,10	$\frac{\partial s_n}{\partial q_1}$	$2D(l_x q_1 + l_y q_2 + l_z q_3)$
0,11	$\frac{\partial s_n}{\partial q_2}$	$2D(-l_x q_2 + l_y q_1 + l_z q_0)$
0,12	$\frac{\partial s_n}{\partial q_3}$	$2D(-l_x q_3 - l_y q_0 + l_z q_1)$
0,13	$\frac{\partial s_n}{\partial D}$	$l_x(q_0^2 + q_1^2 - q_2^2 - q_3^2) + 2l_y(q_1 q_2 - q_0 q_3) + 2l_z(q_1 q_3 + q_0 q_2)$
1,3	$\frac{\partial s_e}{\partial p_e}$	1
1,4	$\frac{\partial s_e}{\partial v_e}$	Δt
1,5	$\frac{\partial s_e}{\partial a_e}$	$\frac{\Delta t^2}{2}$
1,9	$\frac{\partial s_e}{\partial q_0}$	$2D(l_x q_3 + l_y q_0 - l_z q_1)$
1,10	$\frac{\partial s_e}{\partial q_1}$	$2D(l_x q_2 - l_y q_1 - l_z q_0)$
1,11	$\frac{\partial s_e}{\partial q_2}$	$2D(l_x q_1 + l_y q_2 + l_z q_3)$
1,12	$\frac{\partial s_e}{\partial q_3}$	$2D(l_x q_0 - l_y q_3 + l_z q_2)$
1,13	$\frac{\partial s_e}{\partial D}$	$2l_x(q_0 q_3 + q_1 q_2) + l_y(q_0^2 - q_1^2 + q_2^2 - q_4^2) + 2l_z(q_2 q_3 - q_0 q_1)$
2,6	$\frac{\partial s_d}{\partial p_d}$	1
2,7	$\frac{\partial s_d}{\partial v_d}$	Δt
2,8	$\frac{\partial s_d}{\partial a_d}$	$\frac{\Delta t^2}{2}$
2,9	$\frac{\partial s_d}{\partial q_0}$	$2D(-l_x q_2 + l_y q_1 + l_z q_0)$
2,10	$\frac{\partial s_d}{\partial q_1}$	$2D(l_x q_3 + l_y q_0 - l_z q_1)$
2,11	$\frac{\partial s_d}{\partial q_2}$	$2D(-l_x q_0 + l_y q_3 - l_z q_2)$
2,12	$\frac{\partial s_d}{\partial q_3}$	$2D(l_x q_1 + l_y q_2 + l_z q_3)$
2,13	$\frac{\partial s_d}{\partial D}$	$2l_x(q_1 q_3 - q_0 q_2) + 2l_y(q_2 q_3 - q_0 q_1) + l_z(q_0^2 - q_1^2 - q_2^2 + q_3^2)$

the INS/LRF unit, the BNO055 was placed directly behind the LiDARLitev2 on the laser axis so that the two sensors could be easily superimposed mathematically within the device code (Figure 4.b). Figure 6 and Figures 5.a and 5.b show the complete ENA.

3.5.1 Feedback. An enhanced haptic experience is created by using a small mobile phone vibration motor mounted in the
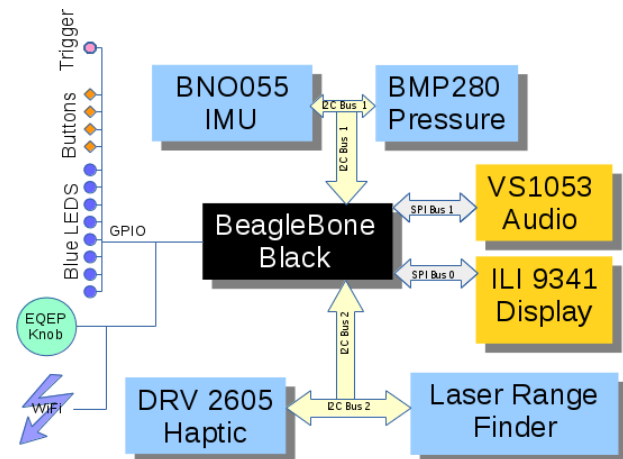

Figure 3. Block diagram of ENA hardware (Graphic by Author)

Table 7

Abbreviated bill of materials

| ID	Component	Description	Manufacturer	Source
1	BeagleBone Black	1GHz TI AM3358B Microprocessor development platform	BeagleBoard.org	Adafruit, New York
2	LiDARLite V2	Laser range finder 100Hz + sample rate, 40m range, I2C	PulsedLight3d (taken over by Garmin)	RobotShop Inc. Vermont
3	BN0 055 development PCB	Inertial Navigation Unit, MEMS type, 9 DOF, with Kalman sensor fusion I2C	Bosch Sensortec	Tindie Pesky Products, California
4	BMP 280	Air pressure sensor I2C, sub component of item 3 PCB	Bosch Sensortec	Tindie Pesky Products, California
5	VLSI Solution vs1053 development PCB	MIDI, Wav and MP3 sound board SPI	VLSI Solution (Finland) / LC Technology (China)	Ebay
6	ILI Technology ILI9341 display	2.2 inch SPI TFT color graphics display 320 x 240	Unknown generic, multiple (China)	Ebay
7	TI DRV 2605 PCB	Haptic driver control, I2C	Texas Instruments, Texas / Adafruit, New York	Adafruit, New York
8	PCB	Full Custom 2-Layer PCB, outsourced fabrication	Dirty PCB, Shenzhen, China	Manufacturer Direct
9	Paintball Trigger Mechanism	Broken for parts electronic paint ball trigger mechanism	Various	II Sports Clearance, Ebay

ENA's pistol grip. A Texas Instruments 2605 DRV motor controller connected to the BeagleBone Black is used to program varying buzzing patterns (Ariza Nunez, Lubos, & Steinicke, 2015). A buzz indicates an obstacle.

Sound feedback is provided by a dedicated VS1053 sound chip to reduce computation loading on the BeagleBone Black (VLSI Solution, 2014). A low pitched MIDI ocarina sound indicates an obstacle further away, while a high pitched sound indicates that an obstacle is close by. No sound means the path is clear.

3.5.2 Powering the Device. Four A123-18650 LiFePO4 batteries located under the pistol grip (Figure 5) are utilized to power the device. The ENA, when running, consumes 5 W. It is conservatively estimated that the total battery life of the ENA ((3.3V * 1.1AH * 4) / 5W = 2.9 hours) is approximately 2 hours.

3.5.3 Printed Circuit Board. I used the computer aided design and manufacturing program KiCAD and the PCB auto-router Free Routing (Kicad, 2016) to design a custom 2-layer surface-mount board. This board was designed as a cape that mates to connectors P8 and P9 of the BeagleBone Black (Coley, 2013). Figures 7.a and 7.b show a KiCAD rendering and subsequent realization of the PCB.

Some of the circuits of the PCB, for example, the SPI Buses (Leens, 2009) that connect
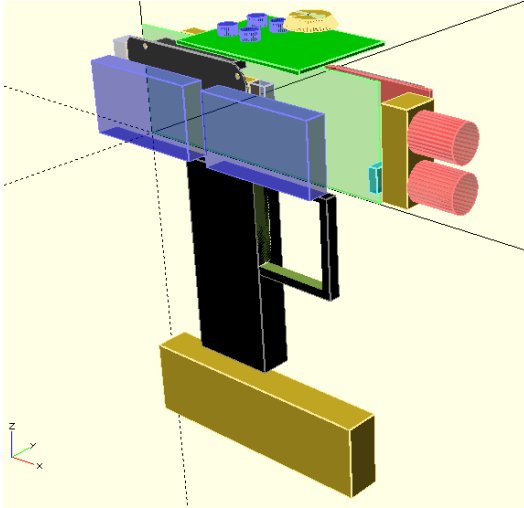
(a) OpenSCAD rendering used to plan ENA component positioning.
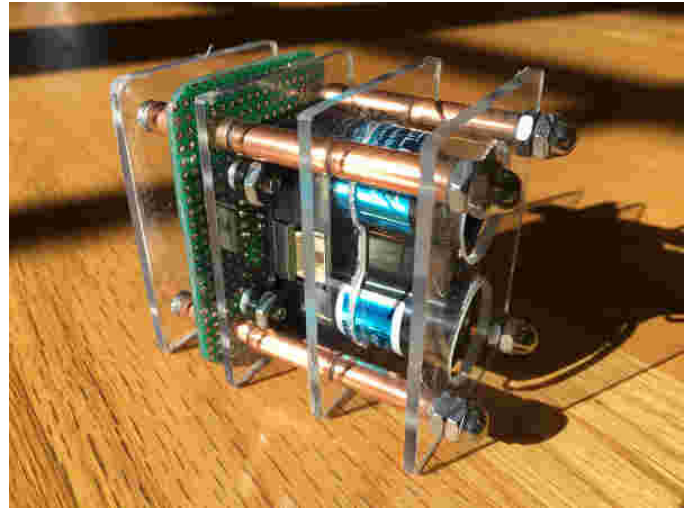
(b) INS on green PCB is laser axis aligned and mounted behind the LRF module. Copper refrigeration plumbing is used as spacers for the polycarbonate structure.

Figure 4. Prototype hardware: initial design and completed component (Graphic and photo by Author)

(a) ILI9341 320 x 240 pixel color display. Low voltage alarm/display is below the grip by the yellow batteries.

(b) Red LED displays showing 5v and 3.3v are part of two switch mode power supplies.

Figure 5. Completed unit side views. Coca-Cola cans are for scale. (Photos by Author)

the ILI9341 display and VS1053 sound processor, run at 8MHz, a sufficiently high speed that needed to be accounted for in the design process. 0.1 μF decoupling capacitors were used to mitigate voltage ripple on integrated circuit supply pins, preventing a reduction in signal headroom and subsequent reduction in noise margins and performance (Analog Devices, 2003). 50Ω resistors were also added in series on the SPI clock lines for impedance matching of PCB tracks to avoid ringing from signal reflections (Semtech International AG, 2006).

Figure 6. Top view: note Lego® buttons with different sizes for easy touch recognition. Power switches on left, anti-shock bungee elastic mounted LRF on right. Velcro attached copper pencil is an auxiliary alignment laser (Photo by Author)
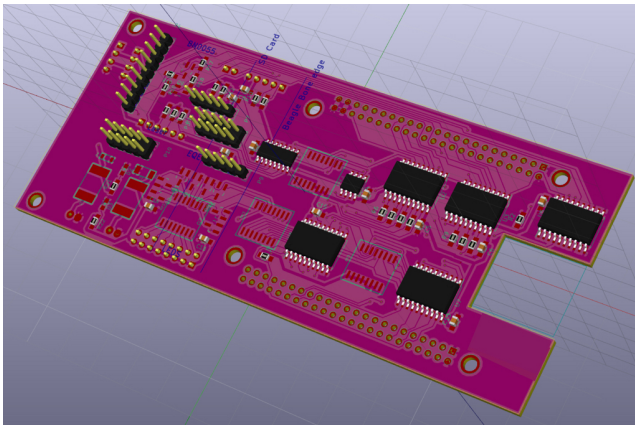
(a) KiCAD surface mount PCB design rendering
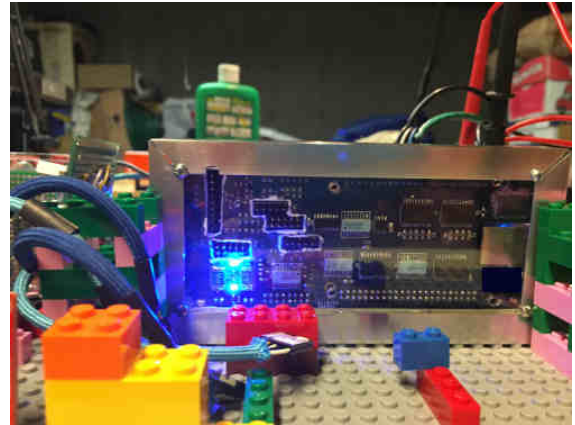
(b) PCB in aluminum frame ready for ENA mounting

Figure 7. Initial PCB design and component realization (Graphic and photo by Author)

3.6   Software

Table 8 lists the software used. The Kalman filter calculations on the BeagleBone Black use the Eigen matrix library (Eigen, 2016) because it allows the use of the ARM® Neon™ SIMD vector by scalar multiplication microprocessor instruction, *VMUL.F32*, thereby improving performance. Extensive use of Unix P-threads (Mueller et al., 1993) improves throughput by scheduling slow input-output data communication tasks from sensors to run concurrently.

Table 8
Software components

ID	Name	Description	Comment
1	Linux version 4.1.6-bone15	Linux kernel for BeagleBone Black (Nelson, 2016)	Linux Hard-float, little-endian
2	Linaro GCC/G++	Cross compiler for BeagleBone Black (Linaro.org, 2016)	
3	Eigen 3	C++ Matrix library (Eigen, 2016)	Uses LAPACK, enables ARM® Neon™ SIMD Instruction
4	LAPACK	Matrix library (Univ. of Tennessee; Univ. of California, Berkeley; Univ. of Colorado Denver; and NAG Ltd., 2016)	Based on C and Fortran codes
5	Adafruit GFX Library	Display graphics library (Adafruit, 2016)	Published for Arduino, ported to BeagleBone Black
6	Adafruit ILI9341 Library	Display graphics library (Adafruit, 2016 B)	Published for Arduino, ported to BeagleBone Black
7	BBB EQEP Library	Controls the EQEP rotation module on the BeagleBone Black (Zapico, 2015)	
8	BBB GPIO Library	Library for fast GPIO switching (Mancuso, 2014)	Uses Linux mmap calls to access hardware directly
9	Adafruit VS1053 Library	Audio sound control library (Adafruit, 2016 C)	Published for Arduino, ported to BeagleBone Black
10	Adafruit DRV2605 Library	Haptic Texas Instruments DRV 2605 control library (Adafruit, 2016 D)	Published for Arduino, ported to BeagleBone Black

3.7   Field Trials

Once the ENA was completed, a series of human subject trials was conducted using seven high school students who volunteered to participate in order to provide both quantitative and qualitative data. This study was previously approved by the Institutional Review Board (IRB) of the high school, and subjects who were minors obtained parental permission to participate. Each subject was instructed to complete an obstacle course, with soft obstacles to avoid injury (Figure 8), under a variety of conditions.

Figure 8.   Obstacle course set up used for human subjects study (Photo by Author)

The course was considered "complete" once a volunteer found all the obstacles in the course. Each obstacle was removed from the course after it was found so that a subject would not locate the same obstacle twice. Subjects completed the course three times: once while blindfolded, once while blindfolded using a cane, and once while blindfolded using the ENA. Their completion times were recorded for quantitative data, and they were given both a pre-experiment and post-experiment questionnaire in order to obtain background data and qualitative feedback.

4 Results and Discussion

4.1 Experimental Setup: Engineering

Three engineering experiments were used to test the finished ENA prototype: (1) a "jitter" experiment to see if the ENA could run at the expected speed, (2) a static experiment to check maximum range and (3) a dynamic moving experiment to check and tune parameters (Table 9) under operational conditions. A UDP network down-link (Postel, 1980) from the ENA to a Linux-Intel host (Figure 9) was implemented to record real-time telemetry data.

4.1.1 Jitter experiment: ENA data rate measurements.

The arrival of each UDP packet was time stamped, and the difference in arrival times t_{diff} was calculated. Figure 10 shows a probability density histogram plot of 30,000 t_{diff} samples. Most are at or near 10 milliseconds, indicating that the ENA's speed performance is as designed.

4.1.2 Static experiment.

Ten simulated detection runs were executed to measure the range of the device. The ENA was mounted on a step ladder (Figure 11.a) at a height of 1.08 meters from the floor with alignment optimized for maximum range. For each run, we recorded the actual spot range based on the floor tape measure and the reported range by the ENA laser range finder. Figure 11.b shows the distribution of the detected ranges, with a mean of 622 cen-
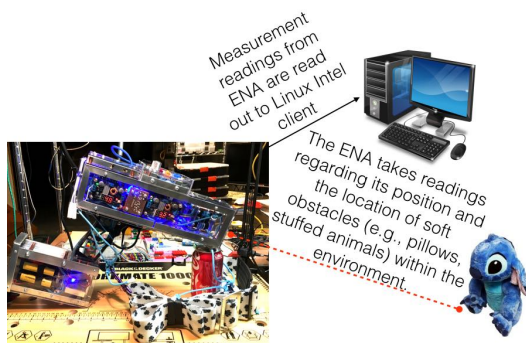

Figure 9. Telemetry down-link (Contains image taken from (Western Illinois University, 2015), graphic by Author)
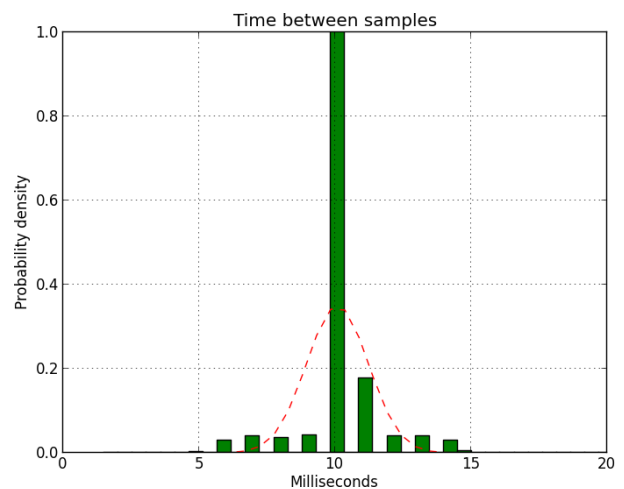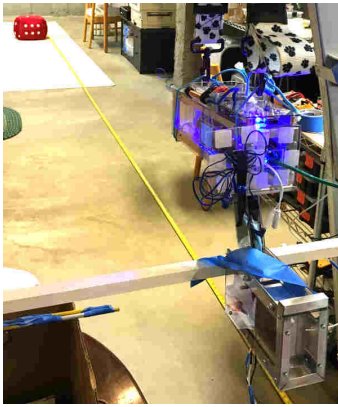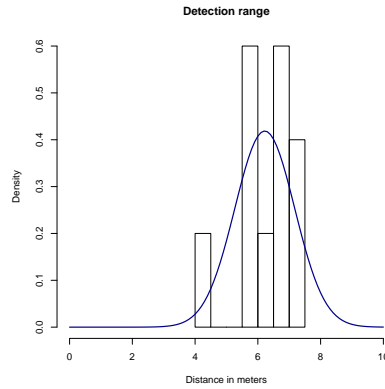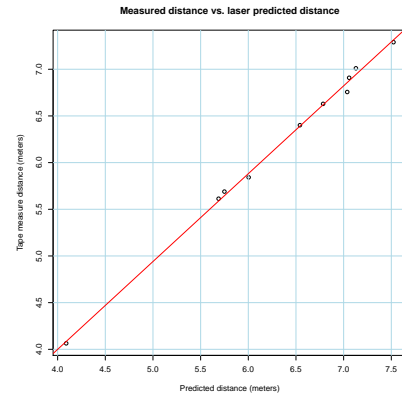

Figure 10. Jitter: distribution of sampling interval times (Chart by Author)

(a) Step ladder static mount (Photo by Author)

(b) Histogram of the measured range with fitted Gaussian. The mean range is 6.22 m. (Graph by Author)

(c) Predicted and observed range. Slope = 0.94, making this nearly a straight line one-to-one relationship. (Graph by Author)

Figure 11. Static range experiment (Figures by Author)

timeters and a standard deviation of 95 centimeters, implying a minimum range[8] of approximately 465 centimeters compared to the 100-150 centimeter range of a typical white cane. Given the ENA's suspended height of 1.08 meters, the observed yellow tape measure floor range vs. that of the ENA's laser reported range was plotted in Figure 11.c with a regression line of Equation 27[9] and a R-squared of 0.9974. Thus, the independent check using the yellow tape measure confirms the ENA's proper performance.

$$y = \underset{(0.10959)}{0.23599} + \underset{(0.01704)}{0.94089}\,x \qquad (27)$$

4.1.3 Dynamic experiment. The ENA was used while recording real-time instrumental data via the UDP down-link. Figure 12 shows a selection of measurement (Table 3), state (Table 2), and resultant surface spot (Equation 24) parameters. Note that the calculated North and East positions tended to be unstable while the Down position was more accurate (Section 3.3.1). While tuning the parameters in Table 9 to minimize latency and optimize response, sometimes the Kalman filter became unstable and diverged if the state noise parameters were set too small. This was because of degenerative conditions that can occur in Kalman filters (Sinopoli et al., 2004). A visualization of the ENA in operation using real-time recorded data is shown in Figure 13.

---

[8]With a confidence level of 95%

[9]Numbers in parentheses indicate the standard error of the regression estimate.
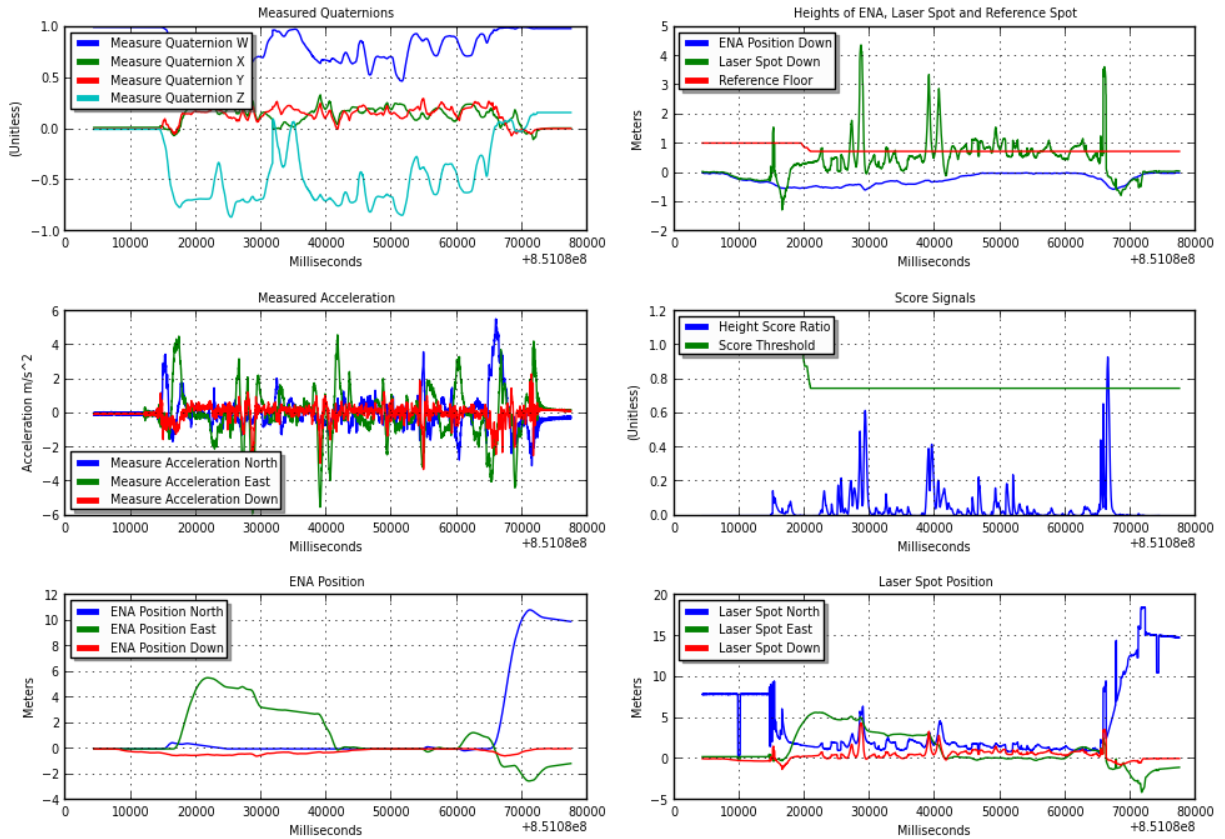
Figure 12. Plots of quaternion, accelerometer, and position from real-time ENA telemetry data. "Measure" means data directly from the BNO055 sensor. ENA Position shows Kalman filter state variables p_n, p_e, p_d (Table 2). Laser Spot Position shows s_n, s_e, s_d from Equation 24. Score Signals are calculated using Equation 26. (Graphic by Author)
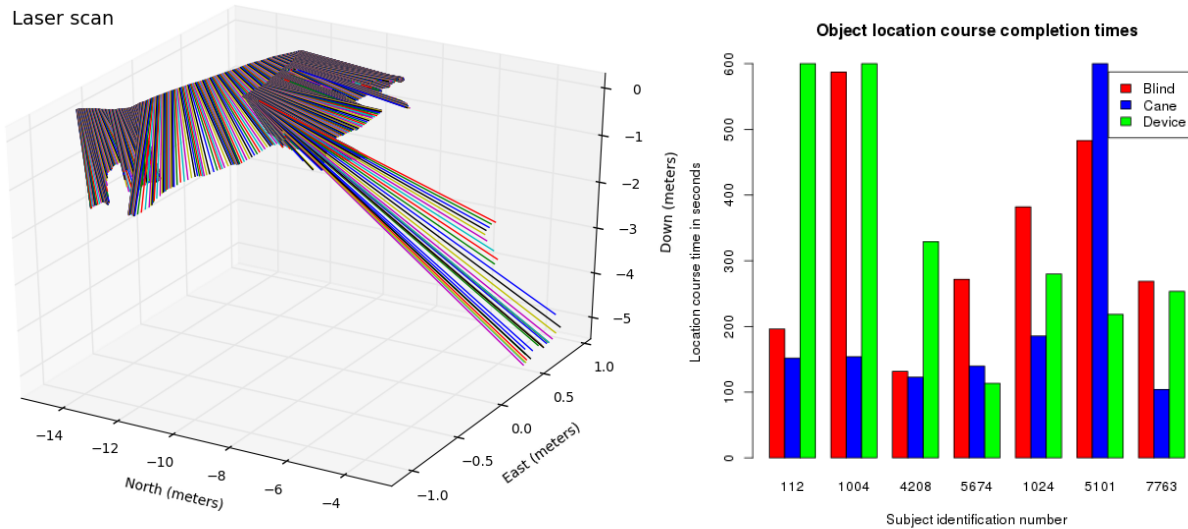

Figure 13. Laser scan visualization created from captured real-time telemetry data. Each line represents a sample. Samples recorded at 100 Hz (Graphic by Author)

Figure 14. Object location course timing in seconds. (Graphic by Author)

Table 9
Typical experimental parameter settings

Variables	Description	Values	Units
$\sigma^2_{n,e,d}$	State acceleration, velocity, and position noise scaling factor (Table 4)	8.0	m/s^2
$\sigma^2_{q_{0,1,2,3}}$	State quaternion noise (Table 4)	2.5	Unit-less
σ^2_{laser}	State laser noise (Table 4)	0.0625	Meters
$\sigma^2_{acc_{n,e,d},m}$	Accelerometer measurement noise (Table 5)	0.08	m/s^2
$\sigma^2_{q_{0,1,2,3},m}$	Quaternion measurement noise (Table 5)	0.0025	Unit-less
$\sigma^2_{q_{laser},m}$	Laser measurement noise (Table 5)	0.000625	Meters
$\sigma^2_{P_d,m}$	Pressure sensor height noise (Table 5)	0.00001	Meters
α	High pass filter parameter (Equation 8)	0.999	Time Constant (Equation 9)
Δt	Sample time step	0.01	Seconds

4.2   Field Trials

The response to the device from subjects was mixed. In quantitative data (Figure 14), it was found that while the device worked very well for some subjects, who took the least time to complete the course while using the device, it did not work as well for other subjects, who took the most time to complete the course while using the device out of all the trials. In qualitative data (Table 10, overleaf), subjects reported that they found the device to be large and heavy. Issues noted included lagging feedback, a frequent need to recalibrate the ENA's Reference Height (h_r, Section 3.4) for the obstacle detection algorithm, and false positives leading subjects to believe obstacles were present in their paths when the paths were actually clear. Because the sample size for these trials was small, more extensive tests will be conducted with a larger sample size. Nonetheless, the acquisition of qualitative data is vital regarding further work to improve the ENA and these preliminary results indicate promise for the future of the device.

4.3   Further Work

There is a need to address three issues for further research. Firstly, the ENA is still too large (45 cm long by 36 cm tall) and heavy ($\approx$ 3 kg). Secondly, the Kalman filter needs better tuning to improve parameter synchronization and reduce measurement latency. Lastly, it may not

Table 10

Field trial results qualitative data. "Purchase cost" is a $US amount that subjects would be willing to pay for the ENA.

Subject identification number	Subject Height (cm)	Purchase cost ($US)	ENA Weight	ENA Size	Recommended Device	Volunteer Comments
112	162.6		Heavy	Big	No	Response little lagging, vibrations moderately intuitive, audio noisy and confusing, too sensitive and detected obstacles that were too far away
1004	157.5	120	A little heavy	Too big	No	Response immediate, vibration moderately intuitive, different sounds for different categories of objects, false positives are confusing
4208	151.3	75	A little heavy	Too big	No	Response little lagging, vibrations not intuitive, audio noisy and confusing, change sound and vibrations to be more indicative
5674	180.0	300	Not heavy at all	Big	Yes	Response immediate, vibrations very intuitive, make it more comfortable
1024	151.0	50	A little heavy	Big	No	Response a little lagging, vibrations not intuitive, audio very intuitive
5101	178.0	400	A little heavy	Big	Yes	Response a little lagging, vibrations very intuitive, audio moderately intuitive, less false positives, instead of trigger should have perfect calibration
7763	177.0	80	Heavy	Too big	Yes	Response immediate, vibrations very intuitive, less false positives, more ergonomic design

be possible for the user to set a floor reference height for the ENA to mitigate drift (Equation 26) in certain environments. A solution to the integrated noise drift problem would allow the removal of the reference height requirement, possibly by incorporating the use of a Global Positioning System (Hide, Moore, & Smith, 2003; Crassidis, 2006; Krakiwsky, Harris, & Wong, 1988).

5   Conclusion

I was able to fulfill all objectives for this study. I created a functional Electronic Navigational Aid prototype that was able to detect obstacles in 3D space without the use of preconfigured infrastructure (e.g., external waypoints). This approach uses an Inertial Navigation System and a Laser Range Finder to measure location in 3D space and distance to obstacles. I successfully filtered sensor noise in my device by combining a Kalman filter algorithm with a high pass filter and pressure sensor, incorporating a stabilizing Zero Velocity Update method to ameliorate bias and noise. Using these techniques, I increased the range of the blind cane by almost 200%, improving situational awareness for users and increasing the safety of navigation. This device, with an improved design, is currently patent pending (Chong, 2016) with the eventual goal of commercial availability and of providing a potentially safer method of navigation for the blind.

6 References

Adafruit. (2016). *Adafruit-gfx-library.* https://github.com/adafruit/Adafruit-GFX-Library.

Adafruit. (2016 B). *Adafruit-ili9341.* https://github.com/adafruit/Adafruit_ILI9341.

Adafruit. (2016 C). *Adafruit_vs1053_library.* https://github.com/adafruit/Adafruit_VS1053\ _Library.

Adafruit. (2016 D). *Adafruit_drv2605_library.* https://github.com/adafruit/Adafruit_DRV2605\ _Library.

Analog Devices. (2003, March). *Decoupling techniques* (No. MT-101). Tutorial.

Ariza Nunez, O. J., Lubos, P., & Steinicke, F. (2015). Hapring: A wearable haptic device for 3d interaction. *Mensch und Computer 2015–Proceedings.*

Bar-Shalom, Y., Li, X. R., & Kirubarajan, T. (2004). *Estimation with applications to tracking and navigation: theory algorithms and software.* John Wiley & Sons.

Borenstein, J., & Ulrich, I. (1997). The guidecane-a computerized travel aid for the active guidance of blind pedestrians. In *Robotics and automation, 1997. proceedings., 1997 ieee international conference on* (Vol. 2, pp. 1283–1288).

Chen, C.-h., Pau, L.-F., & Wang, P. S.-p. (1993). *Handbook of pattern recognition and computer vision* (Vol. 2). World Scientific.

Chong, I. P. (2016, 09 07). *An electronic navigational aid for the blind* (Provisional Patent Nos. US 62/495,236).

Coley, G. (2013). Beaglebone black system reference manual. *Texas Instruments, Dallas.*

Crassidis, J. L. (2006). Sigma-point kalman filtering for integrated gps and inertial navigation. *Aerospace and Electronic Systems, IEEE Transactions on*, *42*(2), 750–756.

Dang, Q. K., Chee, Y., Pham, D. D., & Suh, Y. S. (2016). A virtual blind cane using a line laser-based vision system and an inertial measurement unit. *Sensors*, *16*(1), 95.

Diebel, J. (2006). Representing attitude: Euler angles, unit quaternions, and rotation vectors. *Matrix*, *58*(15-16), 1–35.

Draper, C. S. (1981). Origins of inertial navigation. *Journal of Guidance, Control, and Dynamics*, *4*(5), 449–463.

Durrant-Whyte, H., & Bailey, T. (2006). Simultaneous localization and mapping: part i. *Robotics & Automation Magazine, IEEE*, *13*(2), 99–110.

Eigen. (2016). *Eigen c++ template library.* http://eigen.tuxfamily.org.

Filipe, V., Fernandes, F., Fernandes, H., Sousa, A., Paredes, H., & Barroso, J. (2012). Blind navigation support system based on microsoft kinect. *Procedia Computer Science*, *14*, 94–101.

Foxlin, E. (2005). Pedestrian tracking with shoe-mounted inertial sensors. *Computer Graphics and Applications, IEEE*, *25*(6), 38–46.

Hamilton, W. R. (1844). Ii. on quaternions; or on a new system of imaginaries in algebra. *The London, Edinburgh, and Dublin Philosophical Magazine and Journal of Science*, *25*(163), 10–13.

Hide, C., Moore, T., & Smith, M. (2003). Adaptive kalman filtering for low-cost ins/gps. *The Journal of Navigation*, *56*(01), 143–152.

Kalman, R. E. (1960). A new approach to linear filtering and prediction problems. *Transactions of the ASME–Journal of Basic Engineering*, *82*(Series D), 35–45.

Khairi Abdulrahim, C. H., Terry Moore, & Hill, C. (2014, March). Understanding the performance of zero velocity updates in mems-based pedestrian navigation. *International Journal of Advancements in Technology*, *5*(2). (ISSN 0976-4860)

Kicad. (2016, 7). *Getting started in kicad.*

Kintel, M., & Clifford Wolf, C. (2011). *Openscad, the programmers solid 3d cad modeller.*

Krakiwsky, E. J., Harris, C. B., & Wong, R. V. (1988). A kalman filter for integrating dead reckoning, map matching and gps positioning. In *Position location and navigation symposium, 1988. record. navigation into the 21st century. ieee plans'88., ieee* (pp. 39–46).

Leens, F. (2009). An introduction to i 2 c and spi protocols. *IEEE Instrumentation & Measurement Magazine*, *12*(1), 8–13.

Looney, M. (1995-2016). *Anticipating and managing critical noise sources in mems gyroscopes.*

Mancuso, P. (2014, March). *Beaglebone black bbb c++ api.* https://github.com/petermancuso/bbb.

Mueller, F., et al. (1993). A library implementation of posix threads under unix. In *Usenix winter* (pp. 29–42).

Nelson, R. C. (2016). *Linux kernel for beaglebone black.* https://eewiki.net/display/linuxonarm/BeagleBone+Black.

Noureldin, A., Karamat, T. B., & Georgy, J. (2013). Basic navigational mathematics, reference frames and the earth's geometry. In *Fundamentals of inertial navigation, satellite-based positioning and their integration* (pp. 21–63). Springer.

Postel, J. (1980). *User datagram protocol* (Tech. Rep.).

Praveen, R. G., & Paily, R. P. (2013). Blind navigation assistance for visually impaired based on local depth hypothesis from a single image. *Procedia Engineering*, *64*, 351–360.

Premerlani, W., & Bizard, P. (2009). Direction cosine matrix imu: Theory. *DIY DRONE: USA*, 13–15.

Linaro.org. (2016). *Gcc version 4.9.3.* https://releases.linaro.org/components/toolchain/binaries/latest-5/arm-linux-gnueabihf/.

VLSI Solution. (2014, December). *Vs1053b datasheet* (No. 1.22). Data sheet.

Semtech International AG. (2006). *Rf design guidelines: Pcb layout and curcuit optimization* (No. AN 1200.04). Application Note.

Simon, D. (2006). *Optimal state estimation, kalman, h∞ and nonlinear approaches* (No. ISBN-13 978-0-471-70858-2). Cleveland State University: Wiley-Interscience, John Wiley & Sons, Inc.

Singhal, T., Harit, A., & Vishwakarma, D. (2012). Kalman filter implementation on an accelerometer sensor data for three state estimation of a dynamic system. *International Journal of Research in Engineering and Technology*, *1*(6), 330–334.

Sinopoli, B., Schenato, L., Franceschetti, M., Poolla, K., Jordan, M. I., & Sastry, S. S. (2004). Kalman filtering with intermittent observations. *IEEE transactions on Automatic Control*, *49*(9), 1453–1464.

Smith, J. O. (2008). *Introduction to digital filters: with audio applications* (Vol. 2). Julius Smith.

Soong, G. P., Lovie-Kitchin, J. E., & Brown, B. (2001). Does mobility performance of visually impaired adults improve immediately after orientation and mobility training? *Optometry & Vision Science*, *78*(9), 657–666.

Tamjidi, A., Ye, C., & Hong, S. (2013). 6-dof pose estimation of a portable navigation aid for the visually impaired. In *Robotic and sensors environments (rose), 2013 ieee international symposium on* (pp. 178–183).

Tanigawa, M., Luinge, H., Schipper, L., & Slycke, P. (2008, March). Drift-free dynamic height sensor using mems imu aided by mems pressure sensor. In *Positioning, navigation and communication, 2008. wpnc 2008. 5th workshop on* (p. 191-196). doi: 10.1109/WPNC .2008.4510374

Titterton, D., & Weston, J. L. (2004). *Strapdown inertial navigation technology* (Vol. 17). IET.

Travis, W., Simmons, A. T., & Bevly, D. M. (2005). Corridor navigation with a lidar/ins kalman filter solution. In *Intelligent vehicles symposium, 2005. proceedings. ieee* (pp. 343–348).

UltraCane. (2011). *How to choose the correct length ultracane.*

Ultracane. (2016). https://www.ultracane.com. (Accesed: 2016-11-09)

Understanding quaternions. (2016). http://www.chrobotics.com/library/understanding -quaternions. (Accesed: 2016-05-29)

Univ. of Tennessee; Univ. of California, Berkeley; Univ. of Colorado Denver; and NAG Ltd. (2016). *Lapack – linear algebra package.* http://www.netlib.org/lapack/.

Western Illinois University. (2015). *Computer science.*

Wikipedia A. (2016). *Kalman filter.* https://en.wikipedia.org/wiki/Kalman_filter.

Wikipedia B. (2016). *Atmospheric pressure.* https://en.wikipedia.org/wiki/Atmospheric\ _pressure.

Woodman, O. J. (2007). An introduction to inertial navigation. *University of Cambridge, Computer Laboratory, Tech. Rep. UCAMCL-TR-696*, *14*, 15.

World Health Organization. (2014). *Visual impairment and blindness* (No. 282). http://www.who .int/mediacentre/factsheets/fs282/en/.

Wrigley, W. (1977). History of inertial navigation. *Navigation*, *24*(1), 1–6.

Zapico, J. (2015, Feb). *Bbb eqep library.* https://github.com/jadedanemone/BBB-eQEP.